Soft Matter

ARTICLE TYPE

Cite this: DOI: 00.0000/xxxxxxxxxx

Probing Wrapping Dynamics of Spherical Nanoparticles by 3D Vesicles Using Force-based Simulations†

Didarul Ahasan Redwan,[a] Ke Du[b], and Xin Yong*[a]

Received Date
Accepted Date

DOI: 00.0000/xxxxxxxxxx

Nanoparticles present in various environments can interact with living organisms, potentially leading to deleterious effects. Understanding how these nanoparticles interact with cell membranes is crucial for rational assessment of their impact on diverse biological processes. While previous research has explored particle–membrane interactions, the dynamic processes of particle wrapping by fluid vesicles remain incompletely understood. In this study, we introduce a force-based, continuum-scale model utilizing triangulated mesh representation and discrete differential geometry to investigate particle–vesicle interaction dynamics. Our model captures the transformation of cell membrane shapes and nanoparticle wrapping by calculating the forces arising from membrane bending energy and particle adhesion energy. Inspired by cell phagocytosis of large particles, we focus on establishing a quantitative understanding of large-scale vesicle deformation induced by the interaction with particles of comparable sizes. We first examine the interactions between spherical vesicles and individual nanospheres, both externally and internally, and quantify energy landscapes across different wrapping fractions of the nanoparticles. Furthermore, we explore multiple particle interactions with biologically relevant fluid vesicles with nonspherical shapes. Our study reveals that initial particle positions and interaction sequences are critical in determining the final equilibrium shapes of the vesicle–particle complex in these interactions. These findings emphasize the importance of nanoparticle positioning and wrapping fractions in the dynamics of particle–vesicle interactions, providing crucial insights for future research in the field.

1 Introduction

Recent advancements in nanotechnology have sparked significant interest in the interactions between living organisms and nanoparticles produced from primary and secondary sources [1–3]. Metal and polymer nanoparticles are particularly promising in biomedical research for drug delivery, offering advantages such as targeted delivery and controlled release of therapeutic agents [2,4,5]. Despite these potential benefits, there are growing concerns about the safety of engineered and industrial nanoparticles directly released into the environment. The term "nanotoxicity" refers to the possible harmful effects of nanoparticles on living organisms and represents a significant concern due to their wide range of applications [6–8]. Besides those from primary sources, trillions per liter of secondary nanoparticles can be generated from common consumer plastic products during normal use and many more are produced by environmental degradation of enormous plastic waste [9,10]. Given this concern, there has been a surge in efforts to elucidate how nanoparticles interact with biomembranes and living cells [11–14]. Investigating the intricate dynamics of cellular nanoparticle uptake has been a subject of extensive experimental interest, as evidenced by notable studies [15,16]. Yet, direct observation remains challenging due to the complexity of these interactions and inherent technical constraints. Hence, computational simulations have emerged as a promising tool, shedding light on dynamic processes like nanoparticle encapsulation by cellular membranes [17–21]. In this study, we utilize computational modeling to reveal the intricate dynamics governing the interactions between spherical nanoparticles and three-dimensional (3D) fluid vesicles.

The cell membrane, a lipid bilayer, acts as a selectively permeable barrier that separates the cell from its external environment. For nanoparticles to enter or exit the cell, they must traverse this barrier [22]. Nanoparticle transport modes can be classified into direct penetration through passive diffusion and active translocation based on particle size. Small hydrophobic nanoparticles with sizes of a few nanometers can penetrate the membrane directly via thermal diffusion. Oppositely, particles significantly larger than the membrane thickness resort to energy-

[a] Department of Mechanical Engineering, Binghamton University, Binghamton, New York 13902, United States. E-mail: xyong@binghamton.edu
[b] Department of Chemical and Environmental Engineering, University of California Riverside, Riverside, California 92521, United States.

† Electronic Supplementary Information (ESI) available: [details of any supplementary information available should be included here]. See DOI: 10.1039/cXsm00000x/

intensive transport processes such as endocytosis and exocytosis. During these processes, the membrane substantially deforms and engulfs around the nanoparticles[14,23,24]. Spontaneous wrapping is initiated when the adhesive energy between the nanoparticle and the membrane outweighs the energy penalty associated with bending the membrane to wrap the particle[18]. Continuum-scale models based on Helfrich theory[25] and dynamic triangulated surfaces[26–29] have been predominantly employed to describe cell membrane elasticity and study the interactions of fluid vesicles with nanoparticles. Notably, Bahrami *et al.*[11] as well as Saric and Cacciuto[30] pioneered the investigation of vesicle tabulation triggered by nanoparticle adsorption and ensuing nanoparticle aggregation. These models were later extended to study the wrapping of particles with anisotropic shapes, including ellipsoids, rods, and cuboids[31–33], as well as those with heterogeneous surface chemistry[19].

Recently, modeling studies have expanded to reveal the effects of vesicle properties. Yu *et al.*[20] investigated interactions between nanoparticles and vesicles with different shapes (stomatocytes, prolates, and oblates), systematically characterizing the effects of vesicle volume and membrane curvature on particle wrapping. They also examined cuboid particles and biconcave vesicles to identify the energy-minimized shapes of these vesicles. The same group further predicted phase diagrams for spherical nanoparticles wrapped by vesicles with varying osmotic pressure[21]. Their findings elucidated that the energy barrier of discontinuous envelopment transition increases with increasing osmotic concentration, stabilizing partially wrapped states. Another recent study by Sadhu *et al.*[34] modeled the effect of curvature-inducing proteins on the engulfment of a rigid spherical particle via the Metropolis Monte Carlo algorithm. Their study demonstrated proteins with concave shapes can augment the wrapping process by decreasing the bending energy cost of the membrane and adhering the particle to the surface.

While existing research offers valuable insights into the final equilibrium states of particle–vesicle systems, they predominantly rely on energy minimization techniques[17,34]. In the context of membrane shape optimization, energy minimization involves iteratively adjusting the shape of the membrane to find a configuration where the potential energy of the system is minimized. A considerable shortcoming of these energy-centric methods is their inability to explicitly depict the dynamics of particle interactions and membrane deformations[34]. To probe interaction dynamics, particle-based methods such as molecular dynamics and dissipative particle dynamics are often employed[14,35,36]. Nonetheless, these simulations suffer from limitations in temporal and spatial scales[37,38], hindering their ability to model the wrapping dynamics on a cellular scale. To bridge this gap, we built a computational framework using triangulated membrane representation and discrete differential geometry to compute forces acting on membrane and particle and accurately simulate the nanoparticle wrapping dynamics by fluid vesicles.

This study focuses on large-scale membrane deformation of fluid vesicles induced by the interaction of particles having comparable sizes, mimicking cell phagocytosis of large particles[39] or nanoparticle interaction with extracellular vesicles. We first simulated the dynamics of a single-particle interaction and wrapping by a spherical fluid vesicle, delving into the interaction energy landscapes and induced shape changes. Both external and internal nanoparticle wrapping processes were examined quantitatively. We then investigated how two initially distant nanoparticles interact with the vesicle, characterizing the energy profiles and the evolution of particle configurations driven by membrane-mediated interactions. Finally, aiming to mimic biologically relevant uptake, we analyzed the impact of nanoparticle positioning during the wrapping process as they interacted with a biconcave-shaped vesicle, a shape reminiscent of a red blood cell.

2 Theoretical Background and Simulation Setup

2.1 Membrane elasticity theory

The continuum theory of membrane elasticity describes the deformation of a lipid bilayer membrane using the Helfrich-Canham-Evans Hamiltonian (referred to as the Helfrich Hamiltonian below)[25,40,41]. The membrane is considered a curved two-dimensional (2D) surface embedded in three-dimensional (3D) space, which exhibits fluid-like behaviors in the plane of the membrane while resisting stretching and bending. The fluidity of biological membranes is attributed to the lateral diffusivity of lipid molecules within the lipid bilayer. The membrane does not contain any memory of the previous shape or configuration, indicating the energy functional is solely dependent on the current geometry[42]. The bending free energy of the membrane can be expressed as a functional of mean curvature H, spontaneous mean curvature H_0, and Gaussian curvature G as follows[43]:

$$E_b = \oint dA \Big\{ 2\kappa_b (H - H_0)^2 + \kappa_G G \Big\} \tag{1}$$

Here, $H = (c_1 + c_2)/2$ and $G = c_1 \cdot c_2$ with c_1 and c_2 representing two principal curvatures. The spontaneous mean curvature H_0 can be influenced by various factors, including embedded proteins and lipid composition asymmetry between the two leaflets. The local elastic properties of the membrane are described by κ_b and κ_G, which represent the bending and Gaussian curvature moduli, respectively. When there is no change in the membrane topology, the Gaussian curvature term can be neglected because the corresponding surface integral remains constant according to the Gauss-Bonnet theorem[44]. The minimization of the Helfrich Hamiltonian thus results in a fourth-order nonlinear partial differential equation that describes the optimized shape of the membrane possessing the lowest bending energy. However, this formidable "shape" equation has only been solved analytically for a limited number of highly symmetric cases[45].

Besides the bending energy, the physical models for 3D vesicles also often include the contributions from surface tension energy E_a and osmotic pressure energy E_v. The area energy can be expressed by the following equation[45,46]:

$$E_a = \kappa_a \frac{(A - A_0)^2}{A_0} \tag{2}$$

Here, A_t and A_0 represent the current and preferred total areas of the membrane, respectively. κ_a is the area expansion modulus that controls the strength of penalty to maintain a preferred

vesicle area[47]. A closed membrane also regulates the enclosed volume accordingly. Therefore, we consider the volume energy of the vesicle as[45,46]:

$$E_v = \kappa_v \frac{(V - V_0)^2}{V_0} \tag{3}$$

Here, V and V_0 denote the current and preferred volumes enclosed by the membrane, respectively. The volume constraint modulus, denoted by κ_v, acts as a control parameter that influences how strongly the system penalizes deviations from the desired volume[48]. The volume control term can also be interpreted as the contribution of osmotic pressure when the system is close to the isosmotic condition[21,49]. Thus, the total energy of the vesicle is composed as follows:

$$E_{vesicle} = E_b + E_a + E_v \tag{4}$$

2.2 Calculation of discrete geometric properties

Due to the challenging math involved in solving the shape equation, an alternative approach to the problem of membrane shape optimization is to discretize a smooth surface into a triangulated mesh. Discrete differential geometry[50] is used to calculate the surface geometric quantities necessary for computing the energy functional. We convert a 2D surface M into a triangular mesh network. The mesh consists of vertices V, edges E, and triangles T. Each vertex $v_i \in V$ represents a point on the original surface, and its 3D coordinates determine the shape of the surface. Each triangular element $t_i \in T$ is defined by a group of 3 vertices $(v_i, v_j, v_k) \in V$ sharing a common triangle. In order to compute the bending energy and force, it is necessary to determine the curvatures and surface normal at each vertex of the triangulated surface.

Meyer *et al.*[51] proposed a method to define surface geometric properties at discrete mesh vertices as spatial averages. The averaging process is performed within the immediate neighboring triangles, referred to as the "1-ring neighborhood". Figure 1 provides a schematic representation of the 1-ring neighborhood surrounding a particular vertex i with its position given by a vector $\mathbf{x}_i$. The authors also introduced a mixed vertex area A_{mixed} to ensure a perfect tiling of the surface without overlaps or gaps in the presence of obtuse triangles to minimize the errors originating from spatial averaging. Namely, for a non-obtuse triangle, the vertex area is defined by using Voronoi cells. In contrast, when a triangle is obtuse, its tiling is conducted by using the midpoints of the edges, as shown in Figure 1. Thus, the area of the vertex with the obtuse angle is half of the triangle area, while each of the other two vertices takes a quarter of the triangle area.

The mean curvature of a 2D smooth surface is related to its Laplacian at position $\mathbf{x}$ by the following equation:

$$\Delta_s \mathbf{x} = 2H\mathbf{n} \tag{5}$$

Here, $\mathbf{n}$ is the unit outward normal vector of the surface. Thus, the discrete mean curvature $H(\mathbf{x}_i)$ at a vertex i can be calculated

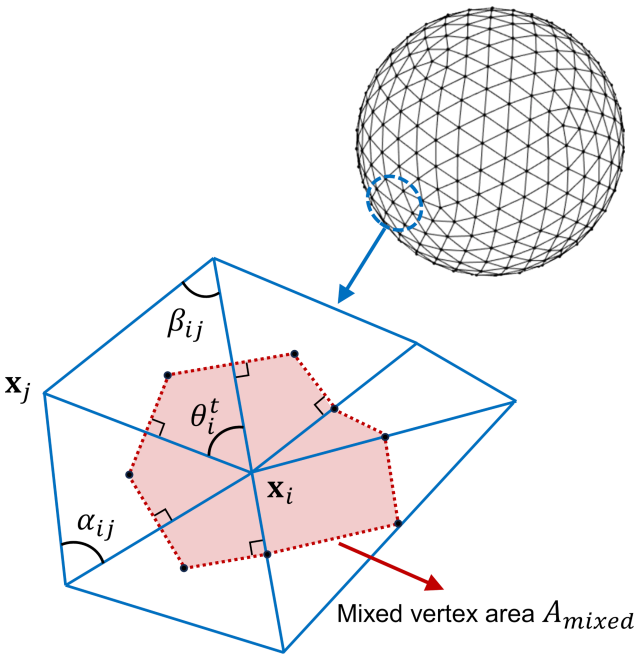

Fig. 1 Schematic diagram of a spherical vesicle mesh and the 1-ring neighborhood of a vertex. The shaded region enclosed by the dashed lines represents the mixed vertex area A_{mixed}.

by the cotangent formula:

$$H(\mathbf{x}_i) = |\mathbf{K}(\mathbf{x}_i)| = \frac{1}{4A^i_{mixed}} \left| \sum_j^{N_v(v_i)} (\cot\alpha_{ij} + \cot\beta_{ij})(\mathbf{x}_i - \mathbf{x}_j) \right| \tag{6}$$

Here, α_{ij} and β_{ij} respectively correspond to the angles opposite to edge $(\mathbf{x}_i, \mathbf{x}_j)$, and $N_v(v_i)$ is the set of 1-ring neighbor vertices of i. The sign of the mean curvature H is determined by whether the direction of the outward normal vector $\mathbf{n}(\mathbf{x}_i)$ matches the sign of the mean curvature vector $\mathbf{K}(\mathbf{x}_i)$ at vertex i. $\mathbf{n}(\mathbf{x}_i)$ can be calculated by the "mean weighted angle" approach[52]. When the signs are the same, the mean curvature is considered positive; otherwise, it is regarded as negative. The discrete Gaussian curvature $G(\mathbf{x}_i)$ can be obtained as a vertex angular deficit by employing the discrete version of the Gauss-Bonnet theorem[51]:

$$G(\mathbf{x}_i) = \frac{1}{A^i_{mixed}} \left(2\pi - \sum_t^{N_t(v_i)} \theta_i^t \right) \tag{7}$$

with θ_i^t representing the angle at vertex i in triangle t. $N_t(v_i)$ is the set of 1-ring neighbor triangles of v_i. Detailed benchmarks of numerical calculations of the mean curvature and the Laplacian of the mean curvature can be found in Section 1 of the Electronic Supplementary Information (ESI) (also see Figures S1 and S2)

2.3 Forces on discretized surface

The bending force acting on each vertex of the triangular mesh can be calculated from the force density vector $\mathbf{f}$, which is given by the first variation of the bending energy functional[53,54]

$$\mathbf{f} = 2\kappa_b \left[2(H - H_0)(H^2 + H_0 H - G) + \Delta_s H \right] \mathbf{n} \tag{8}$$

Here, $\Delta_s H$ denotes the Laplacian of the mean curvature, which again can be calculated by the cotangent expression on discretized surfaces. The nodal bending force is then calculated by multiplying the mixed vertex area with the force density vector evaluated at vertex i

$$\mathbf{f}_b = \mathbf{f}(\mathbf{x}_i) A^i_{mixed} \tag{9}$$

The area constraint force is calculated by taking the negative positional gradient of the energy:[49,55]:

$$\mathbf{f}_a = -\frac{\partial E_a}{\partial \mathbf{x}_i} = -\kappa_a \frac{2(A - A_0)}{A_0} \sum_t^{N_t} \frac{\partial A^t}{\partial \mathbf{x}_i} \tag{10}$$

Here, A^t is the area of the triangle t and N_t is the total number of triangles of the mesh. The discretized form of the area gradient for vertex i is described below[46]:

$$\sum_t^{N_t} \frac{\partial A^t}{\partial \mathbf{x}_i} = \frac{1}{2} \sum_j^{N_v(v_i)} (\cot \alpha_{ij} + \cot \beta_{ij})(\mathbf{x}_i - \mathbf{x}_j) \tag{11}$$

Similarly, the force derived from the volume constraint can be calculated by using the following equations:

$$\mathbf{f}_v = -\frac{\partial E_v}{\partial \mathbf{x}_i} = -\kappa_v \frac{2(V - V_0)}{V_0} \sum_t^{N_t} \frac{\partial V^t}{\partial \mathbf{x}_i} \tag{12}$$

where V^t is the volume of the tetrahedron formed by triangle t and an arbitrary point (selected as the origin here). The volume gradient term can be obtained by the following expression[46]:

$$\sum_t^{N_t} \frac{\partial V^t}{\partial \mathbf{x}_i} = \frac{1}{3} \sum_t^{N_t} A^t \mathbf{n}^t \tag{13}$$

with $\mathbf{n}^t$ being the unit face normal for triangle t.

2.4 Membrane–particle interaction

The adhesion energy between the membrane surface and particle surface regulates the process of particle wrapping by a membrane. We can express the adhesion energy between the discretized surface and the particle as follows[11,31]:

$$E_{ad} = \sum_i^{N_v} V(d_i) A^i_{mixed} \tag{14}$$

Here, $V(d_i)$ is the particle–membrane interaction energy per unit area, which depends on the distance between the vesicle vertices and the surface of the particle $d_i = |\mathbf{x}_i - \mathbf{x}_0| - R_p$ with $\mathbf{x}_0$ representing the particle center and R_p denoting the particle radius. The interaction between particle and membrane can be attributed to electrostatic and van der Waals forces, as well as the binding of specific receptor and ligand molecules anchored in the membrane and on the particle surface. In this study, we model adhesion using a continuous Morse potential[12,17,56]

$$V_M(d_i) = U(e^{-2d_i/\rho} - 2e^{-d_i/\rho}) \tag{15}$$

which is characterized by its depth U and potential range ρ as shown in Figure 2. The potential takes the minimal value of $-U$ at $d_i = 0$, corresponding to the equilibrium distance between the particle and bound membrane patch. Similar to other nodal forces, the adhesion force on each vertex is given by

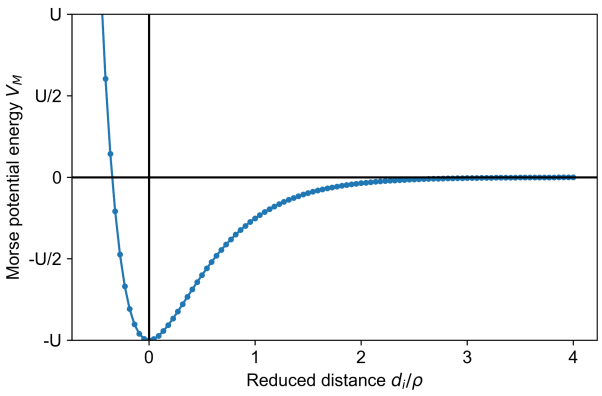

Fig. 2 Energy profile of the Morse potential.

$$\mathbf{f}_{ad} = -\frac{\partial E_{ad}}{\partial \mathbf{x}_i} \tag{16}$$

The total energy of the system including the contribution from the adhesion energy is

$$E_{total} = E_{vesicle} + E_{ad} \tag{17}$$

By comparing the adhesion energy to the bending energy, we can define a reduced adhesion energy $u = UR_p^2/\kappa_b$, governed by bending modulus κ_b, adhesion energy density U, and particle radius R_p. Previous studies have shown that particle wrapping by cell membrane is influenced by the relative curvature C_r and u and $u = 2$ serves as a critical point corresponding to the transition between wrapped and unwrapped states. Moreover, at $u = 2.0$, the interplay between bending and adhesion energies leads to an energy landscape in which the unwrapped and fully wrapped states have equal overall energies, irrespective of the relative size of the vesicle and nanoparticle[12].

2.5 Time integrator and mesh regularization

The forward Euler method is commonly used in numerical simulations, particularly when solving differential equations that govern the evolution of a system over time. The total force $\mathbf{f}_{total}$ of each vertex is calculated to obtain the vertex velocity $\mathbf{v}$. The new vertex position is given for the following time step.

$$\mathbf{v} = \dot{\mathbf{x}} = \mathbf{f}_{total}/\gamma = (\mathbf{f}_b + \mathbf{f}_a + \mathbf{f}_v + \mathbf{f}_{ad})/\gamma \tag{18}$$

Here, γ is an effective drag coefficient representing the strength of viscous dissipation from the background, considering the vesicle is immersed in a liquid. In the context of optimization, the forward Euler scheme is equivalent to the gradient descent algorithm for minimizing an objective function, which herein is the discrete energy.

In simulations with multiple particles, the relative motion between particles during their interaction with the vesicle is of interest. Thus, the particle dynamics is modeled by simply calculating

the reaction force $\mathbf{f}_p$ of the adhesion force according to Newton's third law. Notably, different from $\mathbf{f}_{ad}$ which includes contributions from variations in both Morse potential and membrane vertex area (see Eqs. 16 and 18), the reaction force on the particle accounts for only the contribution from the adhesion potential. To prevent particle overlap, a linear excluded volume repulsion $\mathbf{f}_{ev}$ is also introduced. The particle velocity $\mathbf{v}_p$ is then calculated by $\mathbf{v}_p = (\mathbf{f}_p + \mathbf{f}_{ev})/\gamma_p$ with γ_p being the effective drag coefficient for nanoparticles.

We observed that the triangulated mesh configuration of the vesicle could suffer from significant distortions when interacting with particles, such as elongation in one direction or the generation of obtuse angles. In this force-based scheme, the nodal forces depend sensitively on the underlying mesh geometry. When the mesh structure deforms abruptly, the force variations can lead to numerical instability, convergence issues, or even divergence of the simulation. As a result, the system energy is also significantly affected by mesh quality. To improve simulation stability and ensure the accuracy of the energy analysis, two mesh regularization schemes are implemented. The first regularization scheme is the equiangulation[57], also known as the T2 bond flipping[27]. By using this method, we aim to optimize the triangular configurations of the mesh to achieve equilateral or near-equilateral triangles. The second regularization scheme is the "vertex averaging"[57] to redistribute the vertices to improve the mesh homogeneity. For each vertex, this operation computes a new position by taking the area-weighted average of the centroids of the triangles connected to the vertex. Both regularization schemes play crucial roles in preserving the quality of the triangulated mesh during its evolution. By mitigating mesh distortion and preserving uniform triangular elements, these techniques contribute to more reliable simulations of the particle–vesicle system.

Determining the geometric properties of the triangulated surface of the vesicle constitutes a pivotal component in the computation of force and energy terms. To increase computational efficiency, we utilized the libigl C++ library for the geometric calculations[58]. The simulations were performed by in-house C++ code.We performed a comprehensive validation of our model by reproducing previously observed phase diagrams of vesicle shapes as detailed in ESI Section 2 and Figures S3 and S4.

3 Results and Discussion

3.1 Interactions of single particles with spherical vesicles

Endocytosis and exocytosis are cellular processes involved in the transport of colloidal particles across cell membranes[59,60]. Endocytosis is the process by which a cell takes in substances from its surroundings. Exocytosis, on the other hand, helps the cell release substances into the external environment. To mimic these two processes, we explore the interaction of vesicles with external and internal particles. Particles of different sizes are denoted by a signed vesicle-to-particle relative curvature $C_r = \pm R_p/R_v = \pm R_p$ for the vesicle with initial radius $R_v = 1$. This geometric property reflects the degree of concavity or convexity of the local membrane patch around the initial contact point. The membrane of a spherical vesicle has consistent concavity or convexity, depending on the side of particle interaction. Thus, the sign also differentiates the particles located inside and outside the vesicle. The positive and negative signs correspond to the particles outside and inside the vesicle, respectively. Our model explores the interaction regime for relative curvatures on the order of 0.1 and the large deformation of vesicles induced by particle interaction.

We note that this study does not distinguish real intracellular and extracellular environments separated by membranes with asymmetric lipid composition between leaflets[61] and transmembrane electrostatic potential differences[62]. The current model can be extended to incorporate non-zero membrane spontaneous curvature and asymmetric particle interaction potential depending on the side of the interaction. However, integrating molecular dynamics simulations capturing detailed interactions and/or experimental data is needed to account for these effects accurately, which is beyond the scope of this work.

Due to the use of continuous Morse potential with a finite potential range, we introduce an effective wrapping fraction of the nanoparticles based on adhesion energy to quantify the wrapping state. Namely, it is defined by the ratio of the adhesion energy E_{ad} computed in the simulation to the theoretical adhesion energy corresponding to the wrapping of the entire particle, given as $\chi_{eff} = E_{ad}/\left(4\pi U R_p^2\right)$. When first exploring single-particle interactions, instead of the fixed space frame in which particle dynamics are explicitly modeled, the moving body frame is simulated with the nanoparticle fixed during the wrapping. We confirmed that the selection of different frames of reference has a negligible influence on the system evolution and equilibrium energy. The simulation parameters are given in Table 1.

Table 1 Model parameters used for nanoparticle–vesicle interaction simulations

Parameters	Values
Spherical vesicle radius (R_v)	1.0
Spontaneous mean curvature (H_0)	0.0
Bending modulus (κ_b)	0.01
Area expansion modulus (κ_a)	1.0
preferred surface area (A_0) 4π	
Volume constraint modulus (κ_v)	0.0 (Spherical vesicles) or 2.0 (Biconcave vesicle)
Particle radius (R_p)	0.2-0.4
Reduced adhesion energy (u)	2.0
Morse potential range (ρ)	0.01
Membrane drag coefficient (γ)	1.0
Particle drag coefficient (γ_p)	100.0
Time step (δt)	0.01

We examine the total and bending energies of the particle-vesicle system to gain quantitative insights into their interactions. The theory predicts significant energy barriers associated with the wrapping of external particles[18]. Therefore, to explore and sample states that are energetically unfavorable, we introduce a harmonic biasing potential, which resembles the ideas of umbrella sampling[63] used in molecular dynamics simulations. This potential adds a restraining force that assists in reaching target wrapping fractions.

Figure 3a plots the total equilibrium energies of the particle–vesicle complex at different wrapping fractions. The profiles exhibit distinct behaviors between internal and external particle

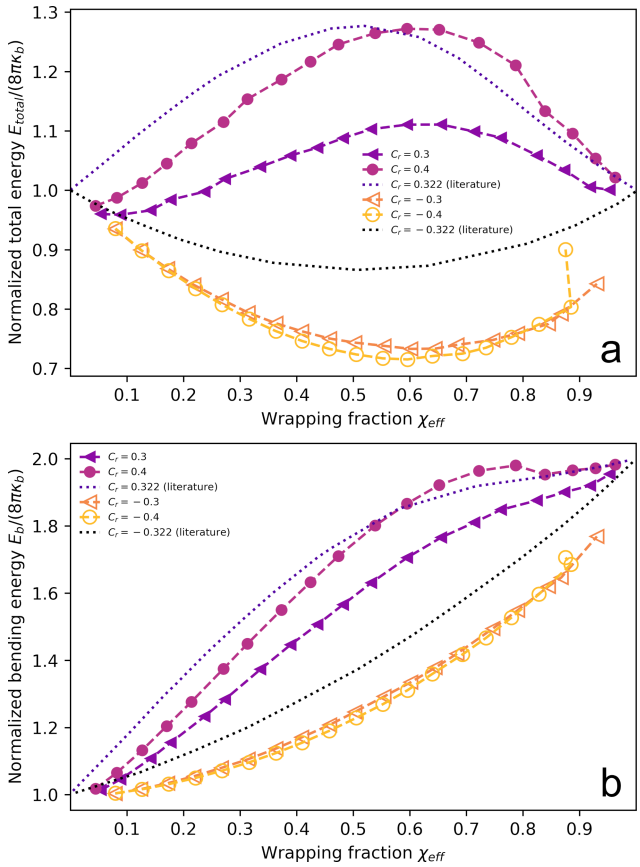

Fig. 3 Normalized (a) total and (b) bending energies as functions of effective wrapping fractions χ_{eff} and relative curvature C_r of the particles. C_r is positive for a particle outside the vesicle (closed markers) and negative for a particle inside the vesicle (open markers). The dotted lines represent theoretical predictions in Bahrami *et al.*[18] for $C_r = \pm 0.322$.

wrapping. For external particles, the total energy first increases and then decreases as χ_{eff} increases. The maximum corresponds to an energy barrier that inhibits spontaneous wrapping. However, if the energy barrier were overcome, the wrapping would proceed until membrane fission to complete the internalization of the fully wrapped particle (not incorporated in the present model). Oppositely, when particles interact with the membrane from the inside, the total energy monotonically decreases until an effective wrapping fraction of approximately 0.6 is reached, indicating spontaneous wrapping. This observation suggests that internal particles naturally affiliate with the membrane. However, additional energy is required to exceed the optimal degree of wrapping. Compared with external wrapping showing pronounced particle size effects, the wrapping of internal particles is significantly less sensitive to the relative curvature, evinced by the collapse of energy curves.

Figure 3b shows the variations in the bending energy of the vesicle induced by particle wrapping. When particles are not wrapped, the bending energies converge to that of an unaltered spherical vesicle, specifically $8\pi\kappa_b$. As the wrapping fraction increases, the bending energies rapidly increase due to the adhesion-induced vesicle deformation. As the wrapping fraction is close to 1.0, the bending energy approaches $16\pi\kappa_b$ regardless of the particle location. This limiting state corresponds to the full wrapping in which two spherical membrane patches are connected by an infinitesimal neck. Notably, external particles induce a steeper bending energy increase relative to those inside. Consistent with the total energy profiles, the particle size has a pronounced effect on external wrapping while the bending energy differences among internal particles are negligible. This observation underscores that external particles exert a more significant influence on vesicle deformation dynamics.

The energy profiles obtained from our numerical model deviate from the theoretical predictions considerably. However, they present features consistent with those observed in other numerical simulations[31]. The most obvious discrepancy between our results and previous theoretical predictions is the significant underestimation of bending and total energies. This deviation is attributed to a key distinction in our methodology compared to that of Bahrami *et al.* While the theoretical calculation relies on a constant free energy per area for adhesion, our model incorporates particle adhesion using a continuous potential defined on a finite range, which results in a varying adhesion energy density, dependent on the instantaneous vertex-to-surface distance. Given this adhesion potential, the particle surface becomes smeared with a broadened attraction range between the particle and the membrane and the particle size effectively increases. These two effects result in increased adhesion energy as well as increased effective wrapping fraction (which is based on the adhesion energy).

Interestingly, the total energy of external wrapping for the smallest particle of relative curvature $C_r = 0.2$ particle (Figure S7) shows a minimum around $\chi_{eff} = 0.2$ in contrast to the theoretical predictions[18], which suggests limited spontaneous wrapping of small external particles. Moreover, the systems cannot reach target wrapping fractions greater than 0.9 and 0.8 for external and internal wrapping, respectively. The energy profiles also exhibit anomalous variations at high wrapping fractions. We assert that this behavior is attributed to insufficient mesh resolutions to accurately capture the high curvature bending induced by the small particles.

Figures S5 and S6 in the ESI showcase the vesicle morphology changes when interacting with external and internal particles, respectively. At low wrapping fractions, vesicles retain a nearly spherical shape. Yet, as χ_{eff} rises, specifically within the range from 0.3 to 0.7, the vesicle undergoes notable deformations both local to the particle as well as in the global shape due to the conservation of membrane area. Depending upon the particle location, the local deformations can adopt either concave or convex configurations. When wrapping a large external particle, the vesicle morphs into a distinct kidney-like shape. In contrast, the vesicles interacting with internal particles predominantly evolve into teardrop shapes as wrapping progresses, consistent among different particle sizes. At $\chi_{eff} = 0.9$, the simulation snapshots clearly show the formation of a neck connecting the membrane patch wrapping the particle to the parent vesicle. Particularly in external wrapping, the neck region resembles a catenoid-like deformation, an exemplary minimal surface with zero mean curvature and thus zero bending energy.

Having observed multiple behaviors hint at mesh resolution,

We further conducted a mesh-sensitivity study to assess the influence of mesh density and particle size on the wrapping state. Our tests utilize a coarser mesh consisting of 5,120 triangles and a finer mesh having 20,480 triangles. Figure S8 demonstrates substantial deviations in the bending and total energy profiles when comparing coarser and finer mesh models for a relative curvature of ± 0.20. The coarser mesh model fails to achieve target wrapping fractions greater than 0.9 and 0.8 for external and internal wrapping of $R_p = 0.2$ particles, respectively. Moreover, the energy profiles exhibit anomalous variations at high wrapping fractions. The finer mesh not only enables the simulations of higher effective wrapping fractions but also results in smoother variations in the energy profiles. For particles with a radius of 0.3 ($C_r = \pm 0.3$) shown in Figure S8, the differences between the two meshes are much less discernible, suggesting the interaction is accurately captured with both mesh resolutions. We note that the total energy for external wrapping plateau at the extreme target wrapping fractions of 0.95, deviating from the further decrease predicted by the theory. Figures S7 and S8 also confirm that the adhesion energy is not affected by the mesh resolution.

To further understand the mesh resolution effect, Figure S9 presents a visual sequence illustrating neck formation in a system with a high wrapping fraction around 0.9. Notably, an intermediate state where the membrane shape is still evolving features an unstable neck morphology, as shown in Figures S9a,b. Theoretically, the neck radius would shrink asymptotically to zero (corresponds to the membrane fission) as the wrapping fraction approaches 1.0. The triangulated surface will inevitably fail to accurately represent the small neck with high curvature, resulting in an overestimation of the mean curvature and bending energy. Consequently, the neck expands unphysically to relieve the excess bending energy as shown in Figures S9c,d, leading to the reduction in the effective wrapping fraction. This improper formation of stable necks of small radii limited by mesh resolution and the finite-ranged particle adhesion could incur a significant energy penalty from the imposed biasing potential. This increased biasing potential energy thus contributes to the rapid increases in the total energy and arrests the system at metastable states as shown by the outlier in Figure 3 and Figure S7.

It is also noteworthy that, for lower wrapping fractions, the deformed vesicle shape remains symmetric around the particle. However, when the vesicle wraps the particle at a high wrapping fraction ($\chi_{eff} > 0.8$), the vesicle deformation becomes asymmetric with concurrent neck formation (See Figures S5 and S6). A comprehensive examination of energy-equilibrium shapes shows that the asymmetric deformation exacerbates when the neck size decreases, corresponding to increasing wrapping fractions. We attribute the development of asymmetric shapes to an uneven distribution of membrane bending force in the neck region. Due to high curvature and non-axisymmetric nodal distribution, the bending force could be highly nonuniform in the transverse direction of the neck and cause the connecting parent vesicle to take an asymmetric configuration to minimize the total bending energy. These findings shed light on the intricate evolution of vesicle morphology in response to particle introduction, further elucidating the interplay between particle size, curvature, and resulting vesicle shapes. Despite external wrapping at extreme wrapping fractions, the interactions of nanoparticles of radius 0.3 are accurately modeled. Thus, we focus on this particle size in the following simulations.

3.2 Interactions of two particles with spherical vesicles

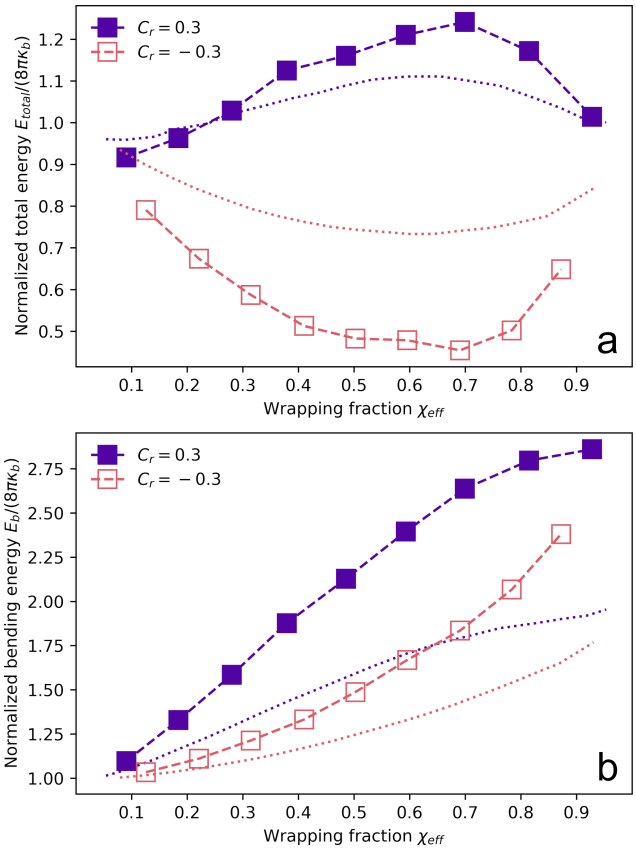

Fig. 4 Normalized (a) total and (b) bending energies of spherical vesicles interacting with two nanoparticles having a relative curvature of 0.3 at different effective wrapping fractions. The solid and open markers represent the states with particles located outside and inside of the vesicle, respectively. Dotted lines present the energy profiles for the corresponding single-particle interaction for comparison. Here, the particle–membrane interaction is modeled by a Morse potential with a reduced adhesion strength of $u = 2.0$ a potential range of $\rho = 0.01$.

In this section, we delve into the dynamics of a spherical vesicle concurrently interacting with two nanoparticles, each with a size parameter of $C_r = 0.3$ at different wrapping fractions. We consider relative particle motion to efficiently probe the interaction dynamics, as described in Section 2.5. As in our previous analyses, we employ the umbrella potential to explore states that are energetically less favorable. Our findings reveal that when a vesicle interacts with two particles, the resulting equilibrium energy profiles (both total and bending) resemble those for the single-particle interactions, as detailed in Figures 4a,b. The bending energies of both external and internal wrapping are significantly higher because the vesicle has to deform more to accommodate extra particles. Compared to a single particle, the external wrapping of two particles needs to overcome a higher energy barrier, while the wrapping of two inside particles is energetically more

favorable. Notably, both the minimum and maximum of the total interaction energy are located at χ_{eff} of approximately 0.7, slightly higher than in the single-particle interactions.

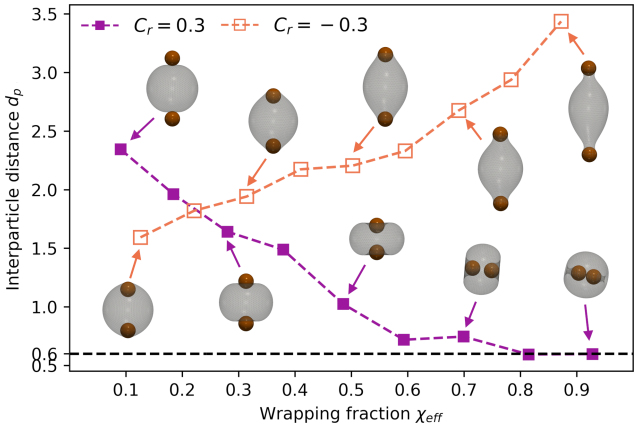

Fig. 5 Relation between interparticle distance and particle wrapping fraction for two particles having a relative curvature 0.3 interacting with a vesicle simultaneously. Insets show corresponding equilibrium configurations for different wrapping states. The adhesion strength and potential range of the particle–membrane interaction is $u = 2.0$ and $\rho = 0.01$, respectively. The dashed line denotes the distance corresponding to the contact of two particles.

We quantify the distances between the two particles as they interact and become wrapped by the vesicle. As shown in Figure 5, for particles within the vesicle, the interparticle distance (d_p) increases proportionally with the increasing wrapping fraction. Concurrently, there is a noticeable elongation of the vesicle, with the particles positioning themselves at opposite poles. Oppositely, during external wrapping, d_p decreases monotonically. Initially, at low wrapping degrees ($0 \leq \chi_{eff} \leq 0.5$), the vesicle appears squeezed by the particles due to the wrapping. However, as the wrapping fraction exceeds 0.5, the vesicle tends to revert to a nearly spherical shape, enclosing the particles within its interior. At very high wrapping fractions, particles approach each other until contact. This close proximity can lead to changes in the vesicle topology through membrane fusion (not accounted for in this study).

In addition to well-separated particles, we also simulated the external wrapping of two adjacent particles. Figure S10 confirms that the vesicle retains a near-spherical shape while interacting with two adjacent spherical particles for lower wrapping fractions. As the wrapping fraction increases, the vesicle first adopts an oblate shape and then recovers a spherical shape once the two particles are completely internalized. Due to enforcing the same wrapping fraction for the two particles, our simulations reproduce the symmetric joint wrapping of two particles observed in previous studies[11]. Notably, in spontaneous interaction in which two particles could have different wrapping fractions, there exists a more energetically favorable state of asymmetric wrapping by an invaginated membrane tube[11].

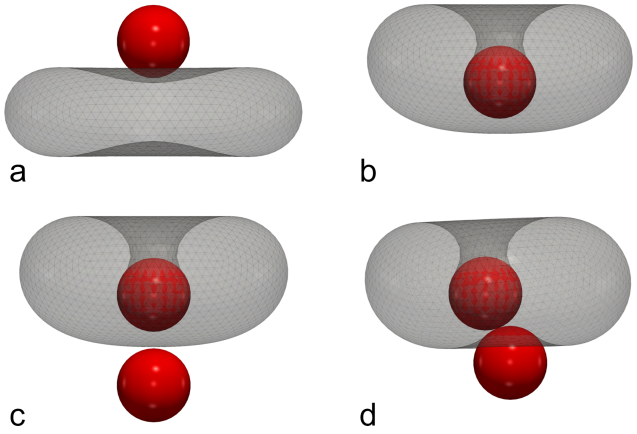

Fig. 6 (a) Initial configuration and (b) well-developed state of a biconcave-shaped vesicle interacting with a single particle. (c) Initial and (d) final equilibrium states of the successive interaction with the second particle are also shown. Particles in red color represent spontaneous interaction without any bias potential.

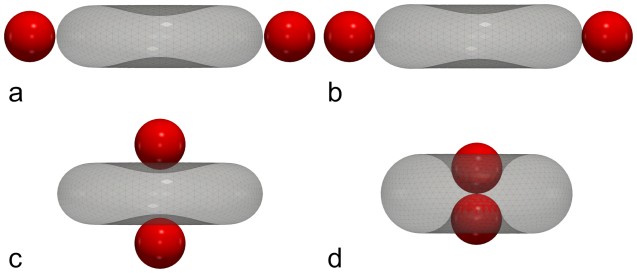

Fig. 7 (a) Initial and (b) equilibrium states of the interaction between the biconcave-shaped vesicle and two particles simultaneously placed at the waist of the vesicle. (c) Initial and (b) equilibrium states when the particles are initially located at the top and bottom concave regions of the vesicle. Particles in red color represent spontaneous interaction without any biasing potential.

3.3 Interactions of particles with biconcave-shaped vesicles

How orientations and initial positions of multiple nanoparticles affect the membrane-particle interaction has been modeled in previous studies, revealing the importance of cooperative effect in multiple particle interactions[64–66]. However, these studies focus on the interaction with membranes with negligible local curvatures (i.e., modeling a flat membrane). In this work, we extend to consider the effect of membrane curvature and further probe the interactions between particles and vesicles with biologically relevant shapes for different sequences and positions of interaction. Due to the extensive interest in cellular responses of nanoparticle exposure, we model biconcave discoid vesicles, which resemble healthy red blood cells (RBCs). Unlike the previous model of spherical vesicles, the biconcave vesicle with a reduced volume of v of 0.65 is subjected to a constant volume constraint with $\kappa_v = 2.0$, mimicking volume regulation in real cells.

We initiate our study by introducing a single particle on the top concave region of a discocyte-shaped vesicle (Figure 6a). The interaction between the particle and vesicle occurs spontaneously without any additional biasing potential. Due to intrinsic membrane concavity at the contact, the membrane rapidly wraps

around the particle as shown in Movie S1 and achieves effective wrapping fractions $\chi_{eff} > 0.8$. The high wrapping fractions confirm the successful uptake of the particle by the cell membrane (Figure 6b). Induced by the particle uptake, the bottom concave region of the vesicle reshapes to a convex shape. After the uptake of the first particle, we position a second particle beneath the vesicle, again without applying any biasing potential (Figure 6c). Interestingly, the second particle archives a significantly lower wrapping fraction around 0.2, while the top particle maintains a similar degree of wrapping during the simulations (Figure 8a).

The difference in the final state is attributed to the morphological changes of the vesicle induced by the first particle. Specifically, the lower concavity of the vesicle disappears which results in an unfavorable interaction between the second particle and a locally convex region of the membrane (imposing a higher energy barrier). In addition, the interparticle distance quickly decreases to $2R_p = 0.6$ (Figure 8a), indicating that the interaction with the vesicle draws two particles into contact. The presence of the highly wrapped first particle thus prevents the further wrapping of the second one. Figure 6d also illustrates the shift of the particles from the vesicle center and the vesicle responds by deforming asymmetrically. Notably, the particle contact would imply the contact of the membrane patches wrapping the particle. We speculate that this membrane contact will lead to membrane fusion and the creation of a hole in the vesicle, corresponding to a topological change. This nontrivial shape transformation could disrupt the structural integrity of the cell and potentially its biological functions, or even induce wrapping-induced lysis.

To further investigate the effect of interaction sequence and local membrane shapes, we place two spherical particles simultaneously in the top and bottom concave region of the discoid vesicle (Figure 7). Figure 7a,b demonstrate that the vesicle fails to uptake the particles positioned at the waist due to the local convexity of the membrane. Namely, the χ_{eff} does not exceed 0.1, indicating a substantial energy barrier imposed by the convex membrane shape. In contrast, the vesicle readily wraps the two particles located near the concave regions of the vesicle (Figure 7c), gradually achieving an intermediate wrapping fraction ≈ 0.45 for both particles, as illustrated in Figure 7d. Figure 8b shows that both particles initially experience a sharp increase in wrapping fraction, which then plateaus, indicating an equilibrium state has been reached. As a result of the concurrent uptake, the interparticle distance decreases until two particles contact (see Movie S2). The vesicle topological change due to the membrane contact would also happen in this case. These results underscore that the outcome of the interaction is influenced by the local membrane curvature. This also highlights that the concavities in biconcave vesicle shape facilitate nanoparticle uptake and emphasize the importance of interaction sequence.

Finally, we explore the dynamics of a discocyte vesicle in the presence of two strongly interacting particles positioned along its waist (see Figure 9 and Movie S3). Here, we impose the umbrella potential to enforce particle wrapping with a target wrapping fraction of 0.5. In the initial phase of simulation (Figure 9a), we observe that the vesicle elongates horizontally to facilitate particle wrapping. Figure 10 registers a corresponding drastic rise in the bending energy. The vesicle transitions to a dog-bone shape. Simultaneously, the particles move apart with d_p increases to approximately 5.4 (Figure 10b). As the simulation progresses (Figure 9b,c), the elongated vesicle begins to contract to release the excess bending energy and move the particles at the two ends of the vesicle toward each other. d_p exhibits a monotonic decrease to approximately 2.8. Approaching equilibrium (Figures 9e-h, the particles aggregate toward the middle section of the vesicle, eventually coming into contact. The vesicle forms a dimple hosting both particles with an effective wrapping fraction of ≈ 0.45 and the bending energy of the vesicle is lowered to 2.25 at the equilibrium (Figure 10) Due to the adhesion energy imposed by particles to deform the vesicle, the equilibrium bending energy is higher than the initial bending energy of the biconcave vesicle. This result showcases the membrane-mediated nanoparticle aggregation on vesicles with complex shapes.

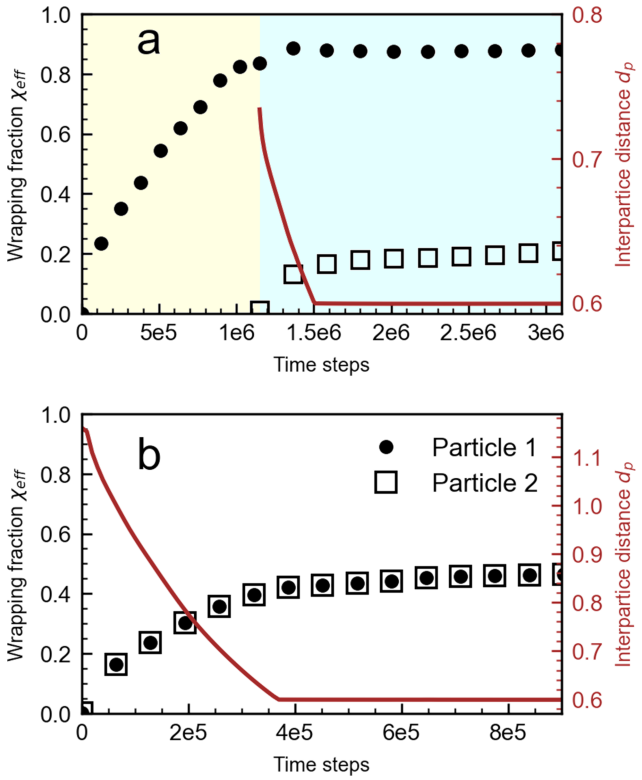

Fig. 8 Temporal evolution of effective wrapping fraction and interparticle distance for two particles, for (a) sequential interaction and (b) simultaneous interaction for two different particles, labeled as Particle 1 and Particle 2. The black markers denote the wrapping fraction while the red line tracks the interparticle distance. The shaded region corresponds to the two stages of the interaction.

4 Conclusions

This study employed a force-based, continuum scale model to investigate the dynamics of fluid vesicles in response to the interactions of nanoparticles that exhibit adhesive interactions and possess dimensions greater than the membrane thickness. The membrane bending energy and total free energy profiles corresponding to the full range of wrapping fractions ($0.05 \leq \chi_{eff} \leq 0.95$)

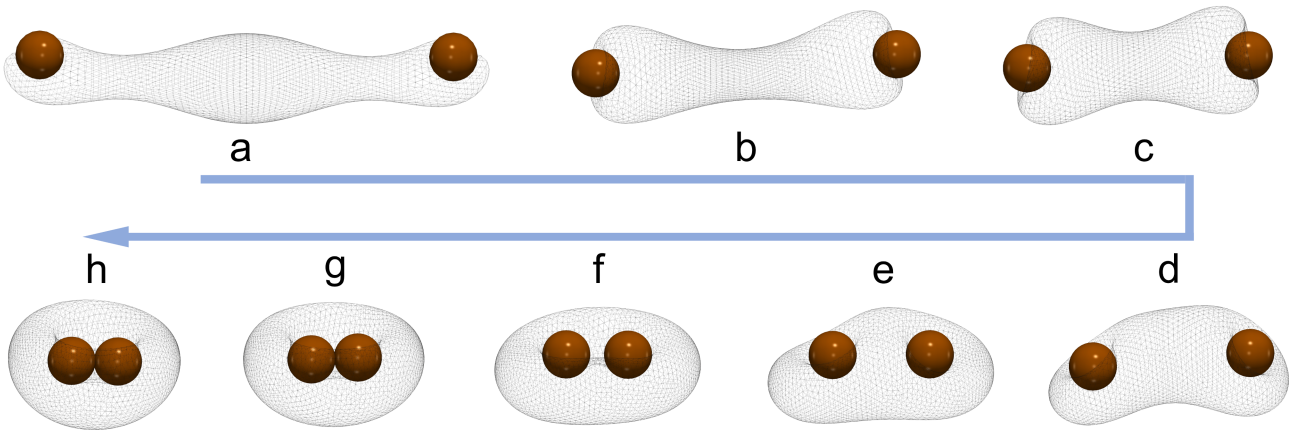

Fig. 9 Simulation snapshot sequence for interaction dynamics between two particles and the biconcave-shaped vesicle with a bias potential to reach target wrapping fraction of 0.5. The initial positions of the particles are on the waist. The brown color indicates the particles with the bias potential.

were systematically characterized for a single nanoparticle interacting with a spherical vesicle at various curvature ratios ($0.2 \leq C_r \leq 0.4$). The results demonstrate that a nanoparticle interacting from outside the vesicle must overcome a substantial energy barrier to achieve full wrapping, whereas an internal particle spontaneously attains an intermediate wrapping fraction. The particle size affects external wrapping more significantly than internal wrapping. Due to the discretization effects, the energy maxima and minima were observed at wrapping fractions higher than 0.5 predicted by the analytical theory[18]. The significant deviations in energies between simulation and theory are attributed to the finite range of the Morse potential used for modeling the particle–membrane interaction. When wrapping an extra particle, the vesicles exhibit similar energy variations, but the magnitudes of energy changes increase. The progressive wrapping of dual particles also results in opposite trends in the interparticle distance for the particles located inside or outside the vesicle. While the wrapping of internal particles drives their separation, the external particles aggregate as being wrapped more.

Furthermore, our research extends to multiple particle interactions with biological vesicles of red blood cell shapes. We elucidate the effects of initial particle positions and interaction sequences in determining the equilibrium configurations of the vesicle-particle complexes. The results show that the membrane concavity facilitates particle uptake while the convex membrane region repels adhesive particles. Vesicle shape changes induced by the interaction of the first particle influence the wrapping of ensuing particles. Finally, the simulation demonstrates highly dynamic shape variations of the biconcave vesicle when interacting with strongly adhesive particles. To conclude, this study highlights the intricacies of particle–vesicle interaction dynamics and reveals the importance of wrapping fractions and particle positioning in governing equilibrium configurations. Our results also provide insights into the potential effects of nanoparticles on biological structures.

Acknowledgements

X.Y. and K.D. gratefully acknowledge funding from the National Science Foundation for supporting this work through awards 2034855 and 2035623. Computing time was provided by the Center for Functional Nanomaterials, which is a U.S. DOE Office of Science Facility, at Brookhaven National Laboratory under contract no. DESC0012704. We would also like to acknowledge helpful discussions with Emad Pirhadi.

References

1 C. Barbe, J. Bartlett, L. Kong, K. Finnie, H. Q. Lin, M. Larkin, S. Calleja, A. Bush and G. Calleja, Silica particles: a novel drug-delivery system, *Advanced materials*, 2004, **16**, 1959–1966.

2 W. H. De Jong and P. J. Borm, Drug delivery and nanoparticles: applications and hazards, *International journal of nanomedicine*, 2008, **3**, 133–149.

3 P. H. Hoet, I. Brüske-Hohlfeld and O. V. Salata, Nanoparticles–known and unknown health risks, *Journal of nanobiotechnology*, 2004, **2**, 1–15.

4 R. Singh and J. W. Lillard Jr, Nanoparticle-based targeted drug delivery, *Experimental and molecular pathology*, 2009, **86**, 215–223.

5 S. Gelperina, K. Kisich, M. D. Iseman and L. Heifets, The potential advantages of nanoparticle drug delivery systems in chemotherapy of tuberculosis, *American journal of respiratory and critical care medicine*, 2005, **172**, 1487–1490.

6 P. R. Leroueil, S. Hong, A. Mecke, J. R. Baker Jr, B. G. Orr and M. M. Banaszak Holl, Nanoparticle interaction with biological membranes: does nanotechnology present a Janus face?, *Accounts of chemical research*, 2007, **40**, 335–342.

7 G. Oberdörster, E. Oberdörster and J. Oberdörster, Nanotoxicology: an emerging discipline evolving from studies of ultrafine particles, *Environmental health perspectives*, 2005, **113**, 823–839.

8 X. Lu, Y. Liu, X. Kong, P. E. Lobie, C. Chen and T. Zhu, Nanotoxicity: a growing need for study in the endocrine system, *Small*, 2013, **9**, 1654–1671.

9 C. D. Zangmeister, J. G. Radney, K. D. Benkstein and B. Kalanyan, Common single-use consumer plastic products release trillions of sub-100 nm nanoparticles per liter into wa-

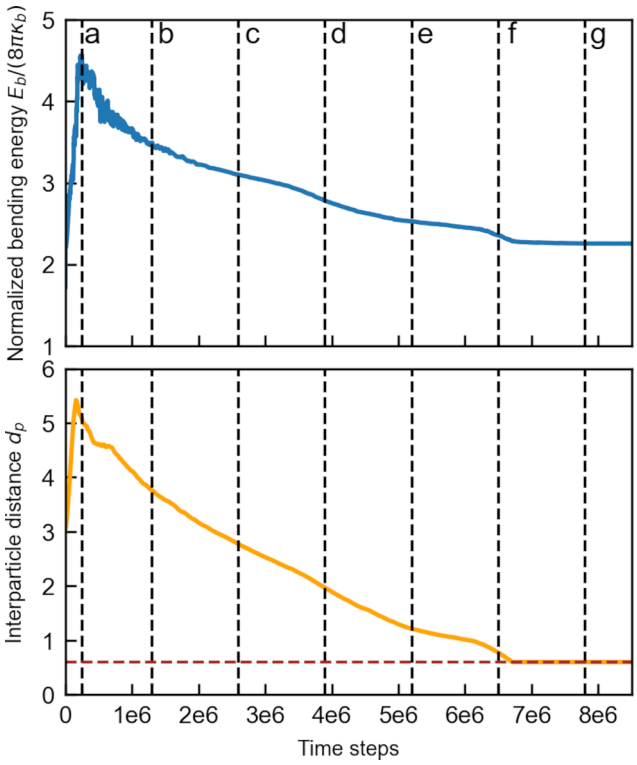

Fig. 10 Evolution of (a) normalized bending energy and (b) interparticle distance for two particles with imposed wrapping fraction of 0.5 interacting with the waist region of the biconcave-shaped vesicle. Labels a, b, c, d, e, f, and g denote specific states corresponding to the snapshots in Figure 9. The dashed line in (b) marks the $2R_p$ distance corresponding to the contact of two particles.

ter during normal use, *Environmental Science & Technology*, 2022, **56**, 5448–5455.

10 J. Gigault, H. El Hadri, B. Nguyen, B. Grassl, L. Rowenczyk, N. Tufenkji, S. Feng and M. Wiesner, Nanoplastics are neither microplastics nor engineered nanoparticles, *Nature nanotechnology*, 2021, **16**, 501–507.

11 A. H. Bahrami, R. Lipowsky and T. R. Weikl, Tubulation and aggregation of spherical nanoparticles adsorbed on vesicles, *Physical review letters*, 2012, **109**, 188102.

12 A. H. Bahrami, M. Raatz, J. Agudo-Canalejo, R. Michel, E. M. Curtis, C. K. Hall, M. Gradzielski, R. Lipowsky and T. R. Weikl, Wrapping of nanoparticles by membranes, *Advances in colloid and interface science*, 2014, **208**, 214–224.

13 F. Zhao, Y. Zhao, Y. Liu, X. Chang, C. Chen and Y. Zhao, Cellular uptake, intracellular trafficking, and cytotoxicity of nanomaterials, *small*, 2011, **7**, 1322–1337.

14 X. Yong and K. Du, Effects of Shape on Interaction Dynamics of Tetrahedral Nanoplastics and the Cell Membrane, *The Journal of Physical Chemistry B*, 2023, **127**, 1652–1663.

15 Y. Goh, Y. H. Song, G. Lee, H. Bae, M. K. Mahata and K. T. Lee, Cellular uptake efficiency of nanoparticles investigated by three-dimensional imaging, *Physical Chemistry Chemical Physics*, 2018, **20**, 11359–11368.

16 V. Belli, D. Guarnieri, M. Biondi, F. Della Sala and P. A. Netti, Dynamics of nanoparticle diffusion and uptake in three-dimensional cell cultures, *Colloids and Surfaces B: Biointerfaces*, 2017, **149**, 7–15.

17 M. Raatz, R. Lipowsky and T. R. Weikl, Cooperative wrapping of nanoparticles by membrane tubes, *Soft Matter*, 2014, **10**, 3570–3577.

18 A. H. Bahrami, R. Lipowsky and T. R. Weikl, The role of membrane curvature for the wrapping of nanoparticles, *Soft Matter*, 2016, **12**, 581–587.

19 A. H. Bahrami and T. R. Weikl, Curvature-mediated assembly of janus nanoparticles on membrane vesicles, *Nano Letters*, 2018, **18**, 1259–1263.

20 Q. Yu, S. Othman, S. Dasgupta, T. Auth and G. Gompper, Nanoparticle wrapping at small non-spherical vesicles: curvatures at play, *Nanoscale*, 2018, **10**, 6445–6458.

21 Q. Yu, S. Dasgupta, T. Auth and G. Gompper, Osmotic concentration-controlled particle uptake and wrapping-induced lysis of cells and vesicles, *Nano letters*, 2020, **20**, 1662–1668.

22 L. Y. Chou, K. Ming and W. C. Chan, Strategies for the intracellular delivery of nanoparticles, *Chemical society reviews*, 2011, **40**, 233–245.

23 S. Behzadi, V. Serpooshan, W. Tao, M. A. Hamaly, M. Y. Alkawareek, E. C. Dreaden, D. Brown, A. M. Alkilany, O. C. Farokhzad and M. Mahmoudi, Cellular uptake of nanoparticles: journey inside the cell, *Chemical society reviews*, 2017, **46**, 4218–4244.

24 G. J. Doherty and H. T. McMahon, Mechanisms of endocytosis, *Annual review of biochemistry*, 2009, **78**, 857–902.

25 W. Helfrich, Elastic properties of lipid bilayers: theory and possible experiments, *Zeitschrift für Naturforschung c*, 1973, **28**, 693–703.

26 H. Noguchi and G. Gompper, Fluid vesicles with viscous membranes in shear flow, *Physical review letters*, 2004, **93**, 258102.

27 G. Gompper and D. Kroll, Triangulated-surface models of fluctuating membranes, *Statistical mechanics of membranes and surfaces*, 2004, 359–426.

28 H. Noguchi, Membrane simulation models from nanometer to micrometer scale, *Journal of the Physical Society of Japan*, 2009, **78**, 041007.

29 D. A. Fedosov, B. Caswell and G. E. Karniadakis, A multiscale red blood cell model with accurate mechanics, rheology, and dynamics, *Biophysical journal*, 2010, **98**, 2215–2225.

30 A. Šarić and A. Cacciuto, Mechanism of membrane tube formation induced by adhesive nanocomponents, *Physical review letters*, 2012, **109**, 188101.

31 A. H. Bahrami, Orientational changes and impaired internalization of ellipsoidal nanoparticles by vesicle membranes, *Soft Matter*, 2013, **9**, 8642–8646.

32 S. Dasgupta, T. Auth and G. Gompper, Wrapping of ellipsoidal nano-particles by fluid membranes, *Soft Matter*, 2013, **9**, 5473–5482.

33 S. Dasgupta, T. Auth and G. Gompper, Shape and orientation matter for the cellular uptake of nonspherical particles, *Nano letters*, 2014, **14**, 687–693.

34 R. K. Sadhu, S. R. Barger, S. Penič, A. Iglič, M. Krendel, N. C. Gauthier and N. S. Gov, A theoretical model of efficient phagocytosis driven by curved membrane proteins and active cytoskeleton forces, *Soft Matter*, 2023, **19**, 31–43.

35 X. Yong, E. J. Crabb, N. M. Moellers and A. C. Balazs, Self-healing vesicles deposit lipid-coated janus particles into nanoscopic trenches, *Langmuir*, 2013, **29**, 16066–16074.

36 I. Salib, X. Yong, E. J. Crabb, N. M. Moellers, G. T. McFarlin IV, O. Kuksenok and A. C. Balazs, Harnessing fluid-driven vesicles to pick up and drop off Janus particles, *ACS nano*, 2013, **7**, 1224–1238.

37 T. Idema and D. J. Kraft, Interactions between model inclusions on closed lipid bilayer membranes, *Current Opinion in Colloid & Interface Science*, 2019, **40**, 58–69.

38 K. Xiong, J. Zhao, D. Yang, Q. Cheng, J. Wang and H. Ji, Cooperative wrapping of nanoparticles of various sizes and shapes by lipid membranes, *Soft Matter*, 2017, **13**, 4644–4652.

39 J. A. Champion and S. Mitragotri, Role of target geometry in phagocytosis, *Proceedings of the National Academy of Sciences*, 2006, **103**, 4930–4934.

40 P. B. Canham, The minimum energy of bending as a possible explanation of the biconcave shape of the human red blood cell, *Journal of Theoretical Biology*, 1970, **26**, year.

41 E. Evans and Y.-C. Fung, Improved measurements of the erythrocyte geometry, *Microvascular research*, 1972, **4**, 335–347.

42 M. Deserno, Fluid lipid membranes: From differential geometry to curvature stresses, *Chemistry and Physics of Lipids*, 2015, **185**, 11–45.

43 A. Guckenberger and S. Gekle, Theory and algorithms to compute Helfrich bending forces: A review, *Journal of Physics: Condensed Matter*, 2017, **29**, 203001.

44 K. Crane and M. Wardetzky, A glimpse into discrete differential geometry, *Notices of the American Mathematical Society*, 2017, **64**, year.

45 M. Siggel, S. Kehl, K. Reuter, J. Köfinger and G. Hummer, TriMem: A parallelized hybrid Monte Carlo software for efficient simulations of lipid membranes, *The Journal of Chemical Physics*, 2022, **157**, 174801.

46 X. Bian, S. Litvinov and P. Koumoutsakos, Bending models of lipid bilayer membranes: Spontaneous curvature and area-difference elasticity, *Computer Methods in Applied Mechanics and Engineering*, 2020, **359**, 112758.

47 D. Steigmann, Fluid films with curvature elasticity, *Archive for Rational Mechanics and Analysis*, 1999, **150**, 127–152.

48 T. Seifert, O. Zschörnig, J. Arnhold and K. Arnold, Beta-blockers inhibit the modification of low-density lipoproteins by sodium hypochlorite in vitro, *Chemistry and physics of lipids*, 1997, **85**, 13–21.

49 C. Zhu, C. T. Lee and P. Rangamani, Mem3DG: modeling membrane mechanochemical dynamics in 3D using discrete differential geometry, *Biophysical reports*, 2022, **2**, 100062.

50 E. Grinspun, M. Desbrun, K. Polthier, P. Schröder and A. Stern, Discrete differential geometry: an applied introduction, *ACM Siggraph Course*, 2006, **7**, year.

51 M. Meyer, M. Desbrun, P. Schröder and A. H. Barr, Visualization and Mathematics III, Berlin, Heidelberg, 2003, pp. 35–57.

52 S. Jin, R. R. Lewis and D. West, A comparison of algorithms for vertex normal computation, *The visual computer*, 2005, **21**, 71–82.

53 O.-Y. Zhong-Can and W. Helfrich, Bending energy of vesicle membranes: General expressions for the first, second, and third variation of the shape energy and applications to spheres and cylinders, *Physical Review A*, 1989, **39**, 5280.

54 K. Sinha and M. D. Graham, Dynamics of a single red blood cell in simple shear flow, *Physical Review E*, 2015, **92**, 042710.

55 D. Fedosov, B. Caswell and G. Karniadakis, Dissipative Particle Dynamics Modeling of Red Blood Cells, 2010, 183–218.

56 M. Raatz and T. R. Weikl, Membrane tubulation by elongated and patchy nanoparticles, *Advanced Materials Interfaces*, 2017, **4**, 1600325.

57 K. A. Brakke, The surface evolver, *Experimental mathematics*, 1992, **1**, 141–165.

58 A. Jacobson, D. Panozzo *et al.*, *libigl: A simple C++ geometry processing library*, 2018, https://libigl.github.io/.

59 R. Sakhtianchi, R. F. Minchin, K.-B. Lee, A. M. Alkilany, V. Serpooshan and M. Mahmoudi, Exocytosis of nanoparticles from cells: role in cellular retention and toxicity, *Advances in colloid and interface science*, 2013, **201**, 18–29.

60 G. Sahay, D. Y. Alakhova and A. V. Kabanov, Endocytosis of nanomedicines, *Journal of controlled release*, 2010, **145**, 182–195.

61 E. Pirhadi, J. M. Vanegas, M. Farin, J. W. Schertzer and X. Yong, Effect of local stress on accurate modeling of bacterial outer membranes using all-atom molecular dynamics, *Journal of Chemical Theory and Computation*, 2022, **19**, 363–372.

62 L. Wang, Measurements and implications of the membrane dipole potential, *Annual review of biochemistry*, 2012, **81**, 615–635.

63 C. Bartels and M. Karplus, Probability distributions for complex systems: adaptive umbrella sampling of the potential energy, *The Journal of Physical Chemistry B*, 1998, **102**, 865–880.

64 T. Yue and X. Zhang, Cooperative effect in receptor-mediated endocytosis of multiple nanoparticles, *ACS nano*, 2012, **6**, 3196–3205.

65 Z. Yan, Z. Wu, S. Li, X. Zhang, X. Yi and T. Yue, Curvature-mediated cooperative wrapping of multiple nanoparticles at the same and opposite membrane sides, *Nanoscale*, 2019, **11**, 19751–19762.

66 T. Yue, X. Wang, F. Huang and X. Zhang, An unusual pathway for the membrane wrapping of rodlike nanoparticles and the orientation-and membrane wrapping-dependent nanoparticle interaction, *Nanoscale*, 2013, **5**, 9888–9896.